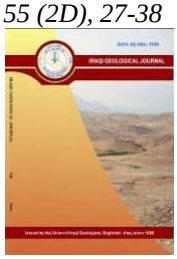
Iraqi Geological Journal

Journal homepage: https://www.igj-iraq.org



Monitoring the Deformation of the Western part of the Nile Delta, Egypt Using Sentinel-1A and Seismicity Data

Mahmoud S. Etman[1], Abdelmonem S. Mohamed[1], Haitham M. Ayyad[2] and Mustafa M. Abu-Bakr[2]

[1] National Research Institute of Astronomy and Geophysics, Helwan, Egypt
[2] Geology Department, Faculty of Science, Al-Azhar University, Nasr City, Cairo, Egypt
* **Correspondence**: mahmoudetman205@gmail.com

Received:
27 March 2022

Accepted:
7 July 2022

Published:
31 October 2022

Abstract

The Egyptian Nile Delta is one of the world's most vital regions owing to its great agricultural, industrial, and economic value. Almost half of Egypt's population resides in this region, which has experienced significant land subsidence during the past decade. The present study evaluates the land deformation rate based on Sentinel-1A C-band synthetic aperture radar imagery on the western part of the Nile Delta. Due to the impact of the earthquake event in crete at magnitude of approximately 6.2 Mw on 19 October 2021, 6 scenes were selected to know the differential interferogram and vertical deformations. In our case study, Sentinel Application Platform processing techniques are applied to 6 Sentinel-1A images on 10 September, 4 October 2021, 13-25 October 2021 and 04-21 November 2021 before and after the occurrence of the earthquake, respectively. Our results show that some places in the western part of Nile Delta region experienced low–medium ground movement. To mitigate the seismic and kinetic effects in the western part of Delta, the construction of large factories near residential areas is discouraged. Moreover, urban expansion should be managed in these regions, and excessive groundwater extraction should be avoided in the arid regions near the western part of Nile delta.

Keywords: Nile Delta; Deformation; Sentinel-1A; Seismic

1. Introduction

The Egyptian Nile Delta is one of the most important residential areas globally. Determining the degree of crustal deformation in the Western Part of Nile Delta is vital to the region's strategy. Several previous studies have identified and discussed the crustal movement in this region. Mohamed et al. (2021); Elsaka et al. (2020) and Saleh et al. (2018) calculated the rate of horizontal movement in the Nile Delta. In addition, Badawy et al. (2005) and Mahmoud et al. (2003) studied the crustal movement and stress fields in Egypt to compare their data with the previous results. The problem under investigation related to evaluate the phenomenon of Western Delta displacement by computing crustal deformation of theWestern part of Nile Delta with regard to the rise of Mediterranean Sea level due to Global warming. The Remote sensing data based on the Sentinel-1A satellite of the European Space Agency, comprehensive variance interference maps and cover dissociation phases are used to evaluate the displacement geocoded and inrefrogram changes. Because of the low coherence pixels, the processing of satellite scenes in agricultural and humid areas varies among periods. This results in

DOI: 10.46717/igj.55.2D.3ms-2022-10-19

limited temporal coverage of the Sentinel 1A satellite images, making an accurate assessment of the subsidence rate impossible. Land used for agricultural purposes in areas surrounding the Western Part of Nile Delta and floodplains of the Nile River has increased recently.

The seismic data are gathered from the Egyptian National Seismic Network (ENSN) and other sources. The crucial objectives of the present study are to estimate the terrain correction and geocoded displacement based on Sentinel 1A images and to compare maps obtained via synthetic aperture radar (SAR) differential interferometry (D-InSAR) in specific periods to enable phase unwrapping. Fig. 1 shows the location map of the survey zone. We analyze the Sentinel-1A data acquired during the fall orbit on 10 September, 4 October 2021, 13-25 October 2021 and 4-21 November 2021 before and after the occurrence of the earthquake in descending using Sentinel Application Platform (SNAP) processing to estimate the defferntial interferogram, terrain correction and geocoded displacement. The results use the SNAP method to improve spatial unwrapping.

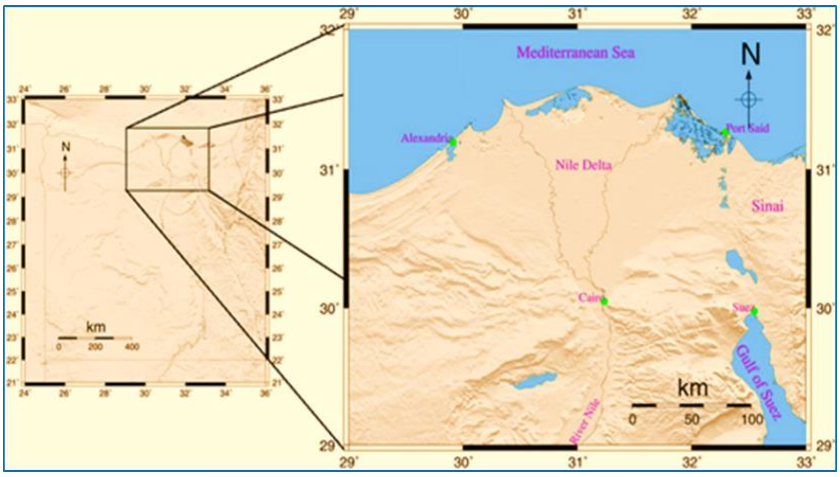


Fig.1. The Surey Zone's Geographical Extent

1.1. Geologic Setting and Seismicity Data

Situated in the southern part of the Nile Cone, the contemporary Nile Delta is a digenetic feature formed by 3500 m of sediment deposited by the Nile and Paleo-Nile water systems over 5 million years (Sestini, 1989). Approximately 60 m of marine sediments accumulated during the Holocene at a 1–7 mm/year rate, which expanded the Egyptian Delta into the Mediterranean Sea at 10 mm/year (Stanley and Warne, 1994) et al. The Nile Delta is divided into four structural sedimentary provinces (Sarhan and Hemdan, 1994): (A) the western desert, which includes stratigraphic sequences and structures in the southern delta region; (B) the northern delta basin; (C) the Nile Cone; and (D) the Levant platform. The Wakar Formation overlies the Sidi Salem Formation and underlies the Rosetta Formation (Nabawy and Shehata, 2015). On a large scale, expected and anthropogenetic impacts have altered the shape of these deltaic systems (Gupta et al.,2008). The Nile Delta is characterized by flat terrain with an 18-meter relief change that progressively slopes northward into the Mediterranean coast (Embabi, 2018; Gebremichael et al., 2018). The Nile fan is the largest alluvial clastic deposit in the eastern Mediterranean Sea, with a distinctive mud-rich marine sedimentary pattern. The Nile Delta was affected by the opening and closing of the Neo-Tethyan Ocean at the African–Arabic Plates' boundaries. The creation of a large rift basin and a passive continental margin in northeast Africa, including northern Egypt, was caused by the late Triassic and early Jurassic extensional tectonics associated with the opening of the Neo-Tethys in the Eastern Mediterranean region. The Nile Delta is divided into two prefectures: the Southern Delta Block (SDB) has a 1–1.5 km thick piece of post-Eocene classics, and the Northern Delta Basin (NDB) contains

a 4–6 km thick section of Neogene sediments separated by an east-west trending "hinge zone" or "hinge line."These studies were conducted on a regional basis in Egypt. The first covers both the onshore and offshore parts of the Delta, and the second focuses only on the onshore section. The goal of this study was not to learn about the architecture of the Wesetern Delta, its tectonic setting, or the differences in crustal thickness inside the transition zone. Moreover, several prior viewpoints conflict with the underlying evidence and exhibit analog configurations. Because of an earthquake in Crete on 19 October 2021 for Mw (6.2), we wanted to know its effect on the study area. To find out the differential interference pattern and the unwrapping phase, we took a pre-quake scenes and a post-earthquake scenes. According to Ali and Badreldin et al. (2019) the dominant fault plane solutions in Dahsour area exhibit normal faulting mechanism with slight and/or large strike-slip movement and stress regime obtained by their study demonstrates a dominant extensional stress trending to NNE–SSW direction. Most of the investigations can practically utilise the direction of the foremost p-wave within the earthquake focal mechanism ponders during the era of 1930–2021, where several significant earthquakes and Fault plane solution occurred around this region (Figs. 2 and 3). The data utilised during this study include the earthquake data.

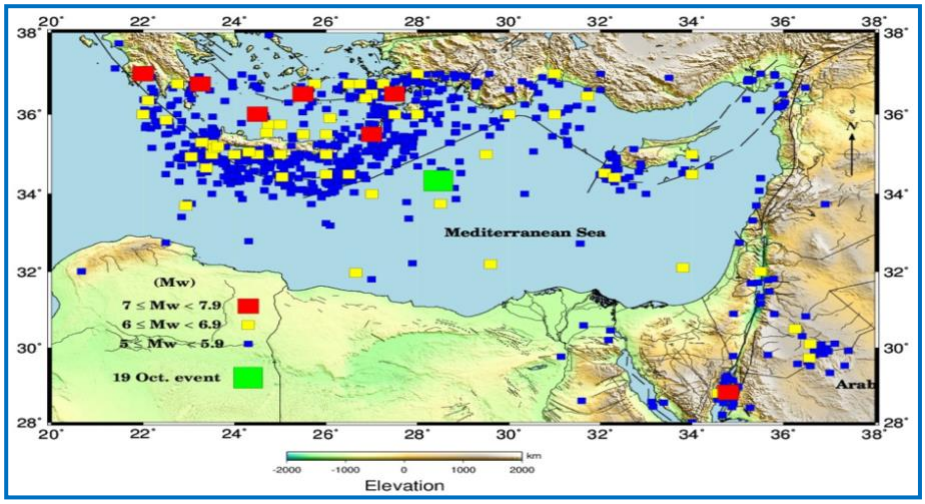


Fig.2. Distribution of seismicity from 1930 to 2021 around the study region, green square is the Crete earthquake which occurred on 19/10/2021.

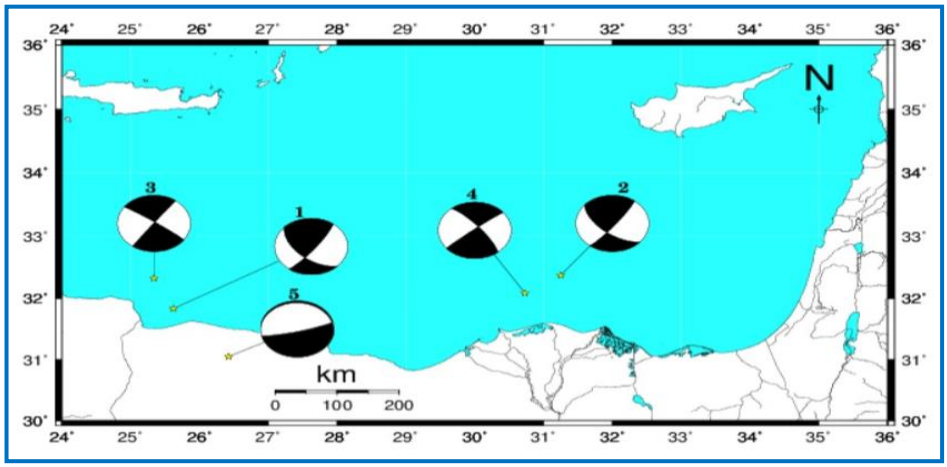


Fig.3. Fault plane solution around the study region (Badreldin et al., 2019).

1.2. Study Area and Data Description

The Western Part of Nile Delta is the region of interest in this study (latitude: 30° 33′ 0″ N, longitude: 31° 27′ 0″ E), with a distance of ~240 km along the Mediterranean Sea. Approximately Six archived single-look complex (SLC) images (track = 131.167; cycle number = 53) recorded by C-band Sentinel-1A sensors on 10 September, 4 October 2021, 13-25 October 2021 and 4-21 November 2021 in descending orbit were used as long-range experimental data this study (Table 1). The available dataset comprised five files containing various descriptive records and was applied to analyze the SLC images. Sufficient datasets enabled a unique image to be selected as the master image for generating temporal interferograms. Fig.4 presents a Quick Look Image of Sentinel-1A including sub_swath (IW1,IW2,IW3) covering the Nile Delta. The SNAP version 6.0, Snaphu v.1.4.2 and Arc GIS V.10.3 are used in.

Table 1. Stack overview and optimal Sentinel-1A InSAR master and slave selection

Satellite	Date/Flight direction	Master/Slave	Track	orbit	Berp	Btemp	M. Coherence
Sentinel-1A	10/9/2021 Descending	Master	167	39614	0	0	1
Sentinel-1A	04/10/2021 Descending	Slave	167	39964	19	-24	0.96
Sentinel-1A	13/10/2021 Descending	Master	131	40103	0	0	1
Sentinel-1A	25/10/2021 Descending	Slave	131	40278	9.41	-12	0.98
Sentinel-1A	04/11/2021 Descending	Master	167	40379	0	0	1
Sentinel-1A	21/11/2021 Descending	Slave	167	40664	86.96	-48	0.88

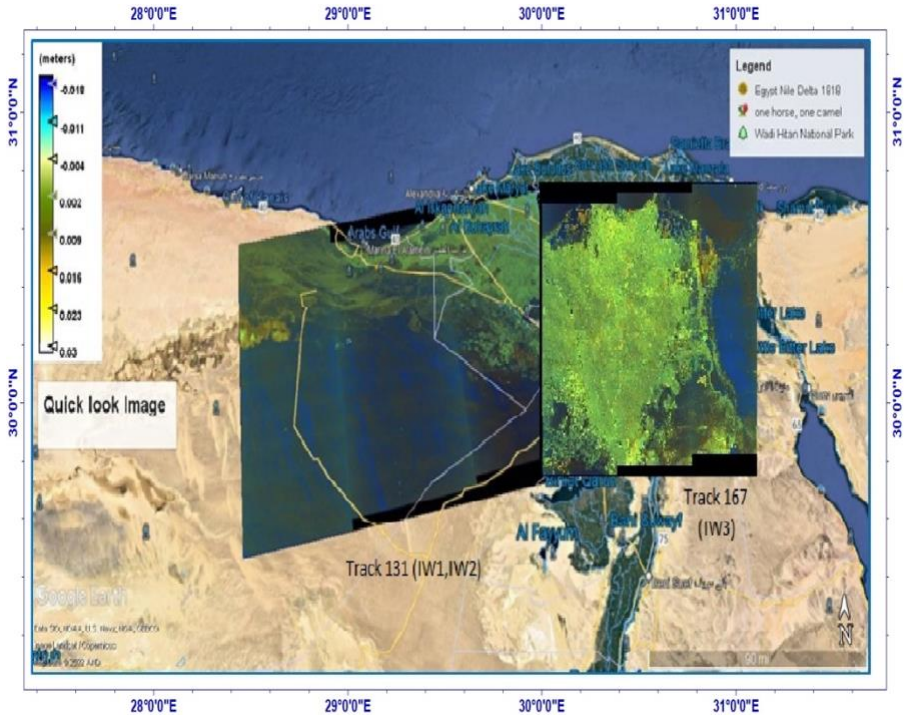


Fig.4. Quick look image of Sentinel-1A including sub_swath (IW1,IW2,IW3) covering the study region for tracks (131,167)

2. Data Methodology and Processing

In this paper, the differential SAR interferometry technique is discussed. These approaches use information from the radar phase of two complex SAR images obtained at different times over the same area and combined to make an interferometric pair. The same sensor or sensors with identical system characteristics are typically employed to gather images across a specified area ; gave the first description of DInSAR, which was based on L-band SeaSat data. The sensor gets an initial SAR picture from a satellite location M using a single-pixel footprint on the ground P. Measure a phase M: (1) M=geom-M+scatt-M=4MP+scat. The phase shift caused by contact is denoted by scattering. Show the DInSAR deformation measurement scheme in Fig. 5.

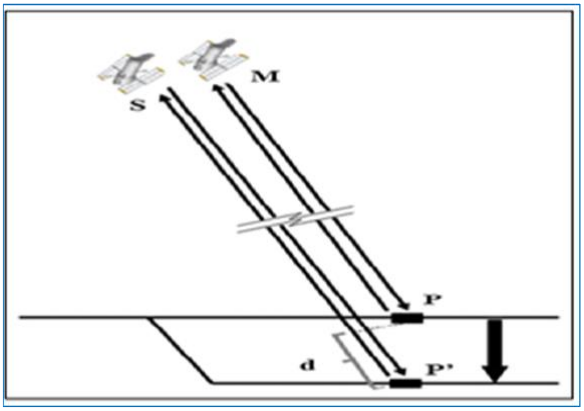


Fig.5. Scheme of DInSAR deformation measurement.

2.1. Image Formation Products

The raw SAR data need to be focused on to produce an image. The focusing is done in the angled variety besides azimuth instructions based on the knowledge of time delay and a combination of backscattered signals from multiple locations, respectively, to create a synthetic large antenna aperture. We used complex I and Q values to represent each pixel image to retain the amplitude and phase information (Zhang et al., 2017). The single lock complex images were selected from the ESA website based on the region's determination, and we chose tracks 131,167. We followed all the IW1, IW2, IW3 Sub- Swaths, and we chose two images that were identified on the same track.

2.2. Coregistration of Data

Coregistration is applied using visual features to align two products with sub-pixel precision (Skakun et al., 2017). Stacking, including both scenes, must be performed to take advantage of different frequencies. SNAP is used to integrate these processes within the S-1 terrain observation by progressive scans (TOPS) co-registration with the enhanced spectral diversity operator. The S-1A back-geocoding procedure registers two differential products using orbit data from various stages and a DEM based on SNAP analysis of Sentinel-1-A data. In this work, all SLCs in each track were successfully co-registered to the master scenes using the approach of Hooper et al. (2007).

2.2.1. TOPS-Split

Only those bursts necessary for the assessment are selected using S-1 TOPS-Split, and each sub-swath is evaluated separately. All sub swaths of each image were separated and divided into IW1, IW2, IW3 and each swath was treated as a separate image from the other, choosing VV polarization, then the rest of the images were made in the same way.

2.2.2. Application of orbit information

SNAP automatically downloads SLC for Sentinel-1 products and adds it to the metadata with an operator that applies orbital files to the data (Braun and Veci et al., 2020). The orbit data encompass information about the satellite situation at DInSAR figures acquisition. The POE files contain 28 h of data and include orbit state vectors of ~10 s in duration. An orbit was applied to each swath, sentinel precise was selected as the state of the orbit, and three polynomial degrees were selected. The rest of the images were made in the same way.

2.3. Interferogram Creation and Coherence Evaluation

The interferometry phase of each SAR image pixel is determined via the resistance throughout the travel impulses from each of the two S-1A and 6 Scenes SARs to the chosen resolution cell. Coherence is regarded as a distinct dot bar that compares the similarity of the secondary and primary scenes on a scale of 0–1. Areas of significant (low) cohesion appear light (dark) in color in the image. In this case, the agricultural patch has low cohesion, and apartment buildings show high cohesion. After generating the co-registration and resampling the slave images to the master scene, interferograms between master and slave scenes were generated. In addition to the deformation signal, the interferogram contains the signal of interest in this study, other signals (owing to atmospheric effects), topographic heights, and other noise sources such as the residual orbital error (Zebker et al., 1997). An interferogram was made for each image, and a digital elevation model (DEM) was selected.

2.4. TOPS Deburst and Subset

The de-burst function is applied to unite all burst operations into a new image. The subset can be applied before phase filtration, and it would be technically possible to achieve the desired effect. The filtered result should be examined before identifying the region of interest. A de-burst has been done to remove the seam-line between all the bursts.

2.5. Goldstein Phase Filtering

The interferogram can be flattened by reducing the topographical phase. Radiation from temporal and spatial deconvolution, volumetric dispersion, and other treatment flaws can cause the interferometric phase to become distorted. However, the specific phase filtering, such as the Goldstein filter, which uses a fast Fourier transform to improve the signal-to-noise ratio of the picture can be applied to increase the quality of the fringes in the interferogram, which is necessary for proper unwrapping in the subsequent step. A detailed description of this filter and its parameters has been presented by Goldstein and Werner et al. (1998). Phase filtering has been applied to each image in the de-burst image, and the output becomes phase filtered the image, and the coherence effect is not present.

2.6. Phase Unwrapping

The interferometric phase can be determined only within a scale of 2π. Interferograms related to the topographical height require initial phase unwrapping. The altitude of ambiguity is determined by the altitude differences that change by 2π after interferogram straightening (Bürgmann et al., 2000). The phase unwrapping solves this ambiguity by integrating phase differences between neighboring pixels (Veci et al., 2015). Integer values of altitudes of ambiguity are deleted. Then, the phase variation between two points on the flatted interferogram is used to measure the actual altitude variation after removing the algebraic quantity of ambiguous elevations. The unwrapping phase has been applied to each photo in 3 steps: 1) Export of the wrapped phase. 2) Unwrapping of the phase. 3) The import of the unwrapping phase. Fig .6 Shows SNAP processing and output steps.

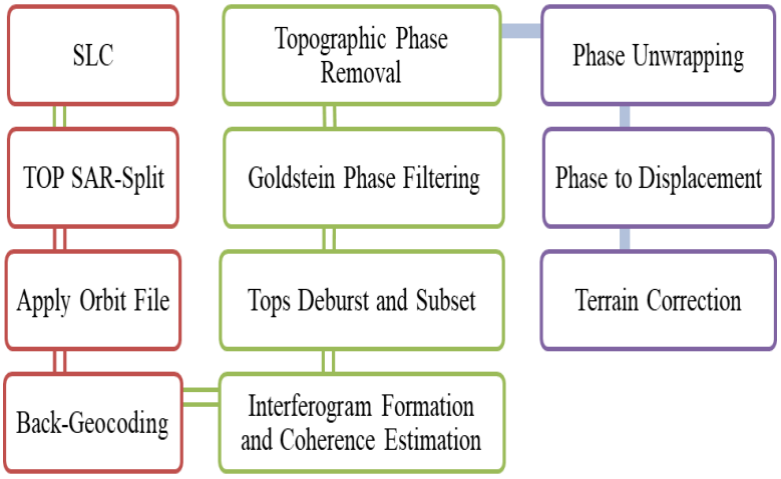


Fig.6. SNAP processing and output steps

3. Result and Discussion

We employed SNAP software to process the data for the Western part of Nile delta area, including two SLC scenes for track131 and four SLC scenes for track 167. In addition, this approach was used with three interferograms to detect coherent and incoherent pixels; thus, one SNAP interferograms were used. The convolution stage was used to remove uncorrelated inaccuracies in the sample image spatial viewing angle and interference. Two co-registered SAR images were differentiated via the complex multiplication of input for each resolution cell. SNAP was used to process interferogram Sentinel-1A data in this project. Fig.7 Shows a) Topographic phase; b) Unwrapped phase; c) Vertical deformation; d) Elevation respectively derived from sentinel 1A (10 September- 4 October 2021) of the study area. The Earth's surface deformation was estimated using the interferometric phase difference. Fig. 8 shows the unwrapped period interferogram of the Nile Delta region (IW1,IW2 sub swath) based on Sentinel-1A data. The fringe pattern is apparent in all interferograms, causing unwrapping inaccuracies. The reliability of unwrapped results is highly dependent on source consistency (Ullo et al., 2019). Although there is no specific threshold, the recommended low coherence value is 0.3. Finally, topographically corrected unwrapped phase values are converted into displacement values. Fig. 9 Shows a) Interferometric phase; b) Unwrapped phase; c) Vertical deformation; d) Elevation respectively derived from sentinel 1A (13-25/10/2021) of the study area. Also, We processed data for a region of the Western part of Nile Delta with SNAP software by using 6 single look complex (SLC) images. three interferograms for SNAP were used to identify persistent and coherent pixels. For the SNAP approach, we computed ten interferograms, and the wrapped phase was corrected for spatially-uncorrelated look angle error and noise associated with the master image. The interferogram is formed by the complex multiplication of the observations in each resolution cell of two coregistered SAR scenes (Master and Slave). All interferograms in this work were created using SNAP Processing for Sentinel-1A Software. Fig.10 Shows a) Topographic phase; b) Unwrapped phase; c) Vertical deformation; d) Elevation respectively derived from sentinel 1A (4-21 November 2021) of the study area. The minimum and maximum vertical displacement were obtained as -0.14 to 0.22 m (Fig.7c), -0.19 to 0.31m (Fig 9c), -0.21 to 0.27 m (Fig 10c) according to InSAR process (Table 2).

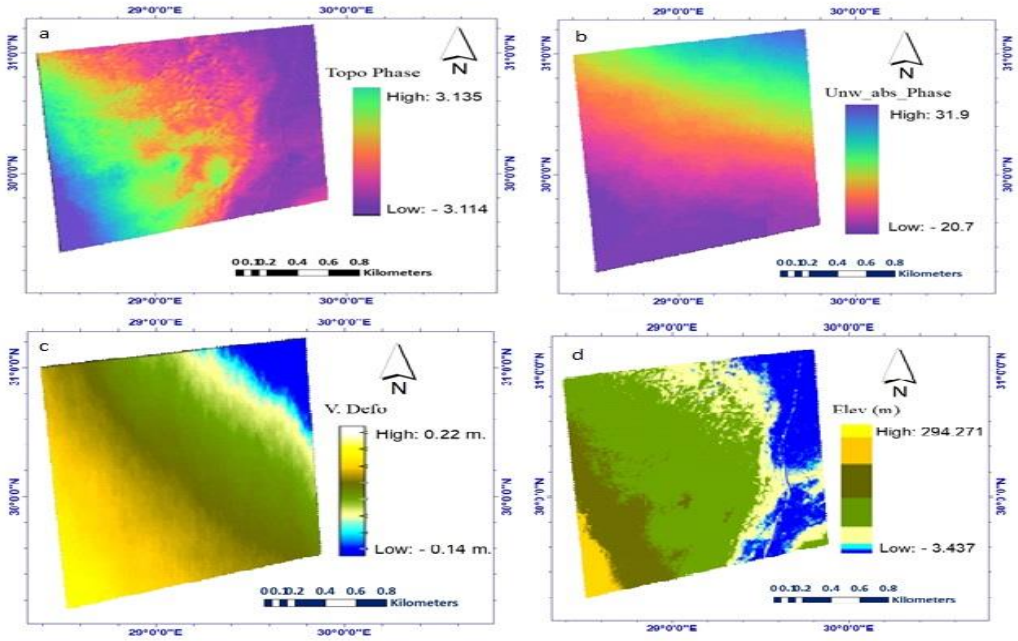


Fig.7. a) Topographic phase; b) Unwrapped phase; c) Vertical deformation; d) Elevation respectively derived from sentinel 1A (10 September - 4 October 2021) of the study area.

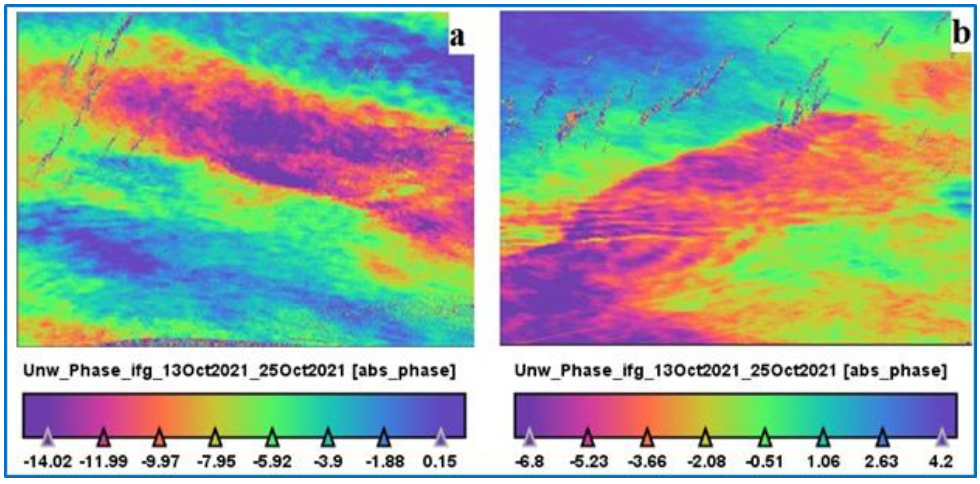


Fig.8. The unwrapped period interferogram of the Western delta region (IW1,IW2 sub swath) based on Sentinel-1A data.

No tremors of magnitude > 5.0 occurred arround Nile Delta region throughout the Sentinel-1A SAR data period on September 10 - October 04, 2021, October 13-25, 2021 and November 04-21, 2021 for track 131 and 167. Therefore, the calculated velocity distribution was unaffected. In the displacement of the spacecraft's radial component, all displacement data are relative to a previously selected stationary point. Most of the Western part of Nile Delta areas appear to be relatively stable, with yellow dots in the figure representing phase to displacement being close to zero. The negative velocities were strongly concentrated in the southern areas of the region. The southern section has a low standard deviation (high resolution), whereas the northern area has a high standard deviation (low accuracy).

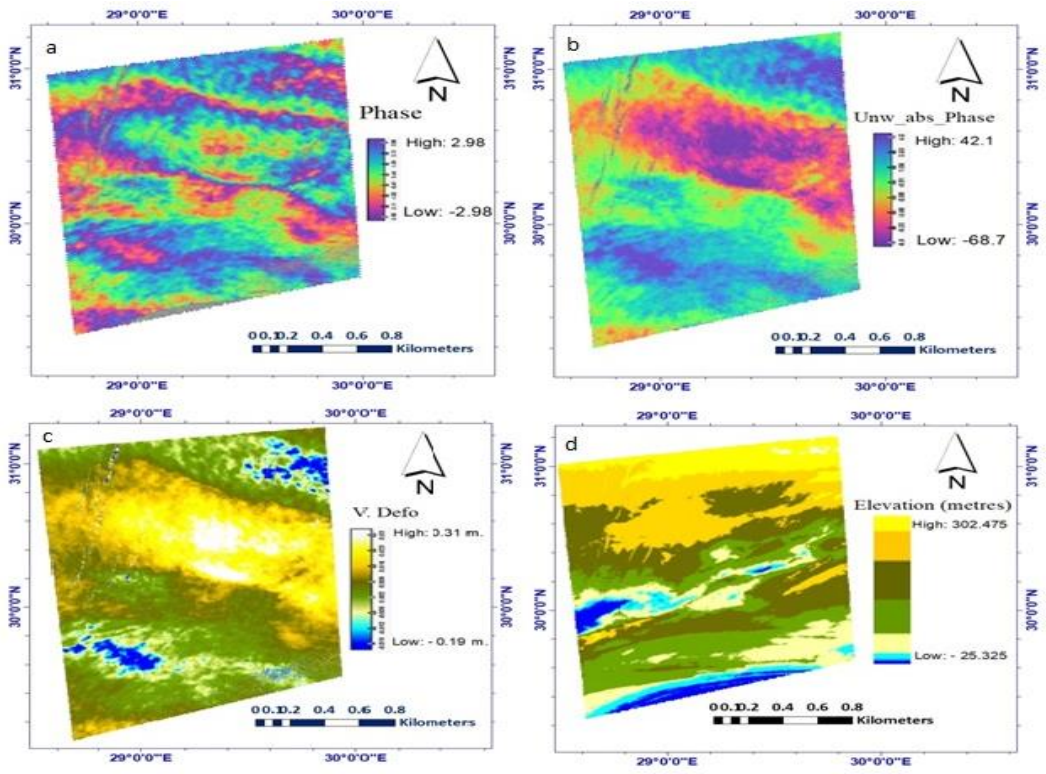


Fig.9. a) Interferometric phase; b) Unwrapped phase; c) Vertical deformation; d) Elevation respectively derived from sentinel 1A (13-25 October 2021) of the study area.

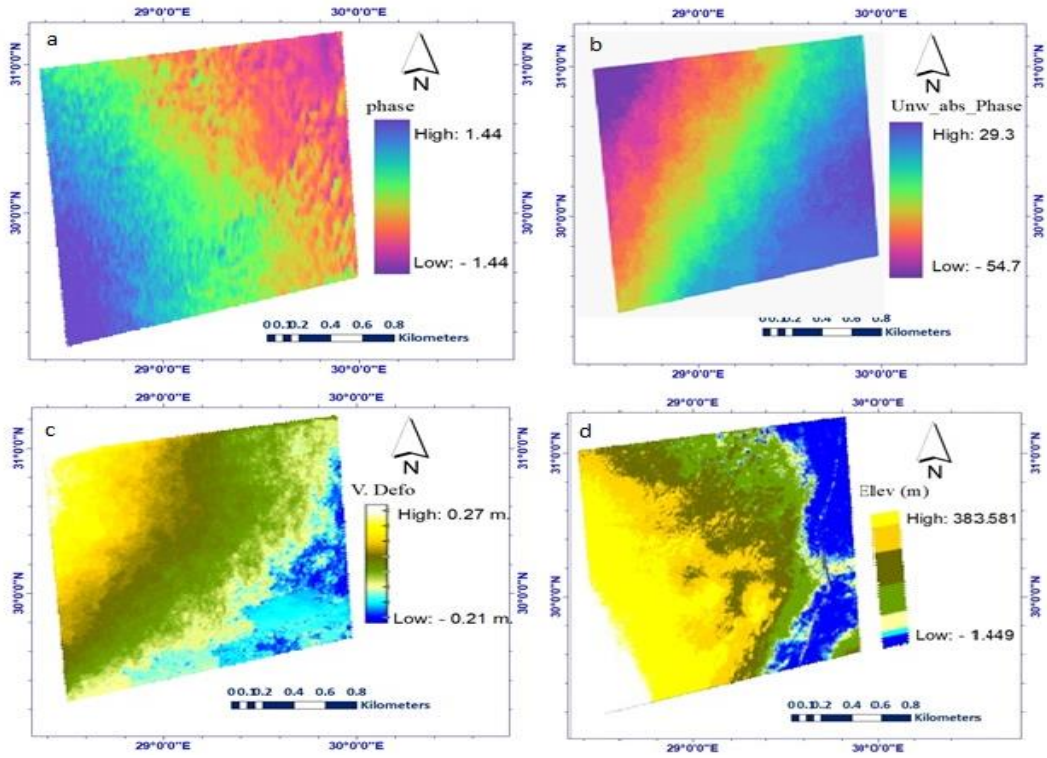


Fig.10. a) Topographic phase; b) Unwrapped phase; c) Vertical deformation; d) Elevation respectively derived from sentinel 1A (4- 21 November 2021) of the study area.

Table 2. Charactristics of Sentinel 1A data and output of scenes used in this study

Charactristics	Wrapped Phase (10 Sep. – 4 Oct. 2021)	Phase (13-25 Oct. 2021)	Phase (4-21 Nov. 2021)	Vertical Deformation (average)
Minimum	-0.2026	-3.1410	-0.4689	-0.1275
Maximum	3.8381	3.1415	3.9410	0.1543
Mean	0.9810	0.3054	0.3390	0.0036
Standard deviation	0.7184	1.7509	0.9478	0.0135
Coefficient of variation	0.7322	5.7324	1.3756	3.6642
Median	0.8519	0.5386	0.2577	0.0012
Max error	0.0040	0.0062	0.00144	2.81E-4
sigma	0.7184	1.750	2.6867	0.0135
avg_scene_height	140.96	113.57	141.325	131.95
DEM	SRTM 3Sec HGT	SRTM 3Sec HGT	SRTM 3Sec HGT	SRTM 3Sec HGT
M.Coherence	0.9610	0.9810	0.8864	0.9428
Height of Amfbiguity	+-672.786	+-1642.77	+-148.103	
Doppler Difference	+-2.19655	+-0.3162	+-1.4521	

Terrain correction geocodes a scene by correcting SAR image noise using a DEM and creating a plot-reflected output, whereas geocoding translates an image from ground range geometry to a map with Cartesian coordinates (Loew and Mauser et al., 2007). The DEM used in terrain geo-coding corrects geometric distortion. Terrain correction and geocode displacement have been done for each image. Shuttle Radar Topographic Mission (SRTM) one second HGT and Bilinear interpolation as input DEM were selected in processing parameters. Also, WGS84 was selected in a map projection. In proper pixel validation, done coherence-vv greater than 1. Fig. 11 Show trrain correction and geocoded displacement raster for two scenes, (a) Wide Swath1(IW1); (b) Wide Swath2(IW2).

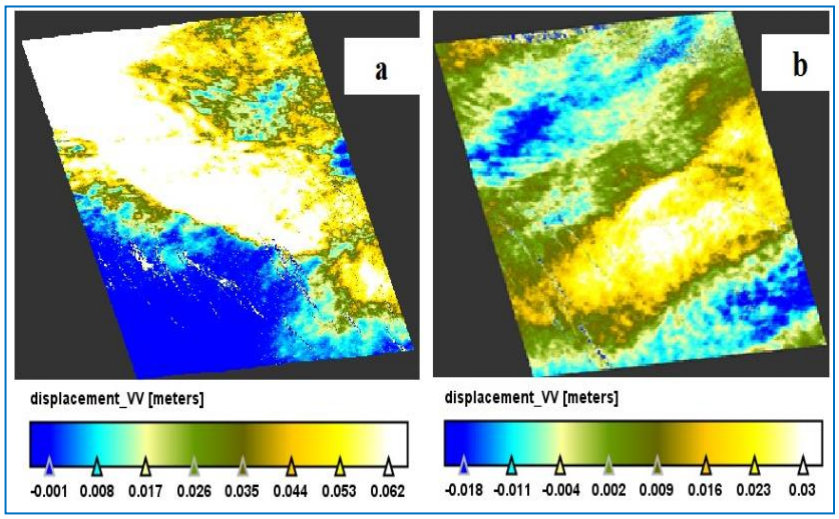


Fig.11. Show trrain correction and geocoded displacement raster for two scenes, (a) Wide Swath1 (IW1); (b) Wide Swath2(IW2) for track 131.

4. Validation of Displacement Calculations from Earthquake Data

Estimating the earthquake sources parameters (e.g rupture length, rupture width, stress drop and displacement) requires the calculation of the seismic moment (M0). The seismic moment is defined by Aki, (1966) as the irreversible deformation of the ground surface. Mathematically the seismic moment can be expressed as shown in Equation 1.

$$M0= \mu AD \quad (1)$$

Where, μ is the rigidity modulus, A is the rupture area and D is the displacement along the fault. seismic moment magnitude scale (Mw) is defined in Equation 2.

$$Mw= 2/3 \log M0 – 10.7 \quad (2)$$

Several empirical scaling relationships are estimated to calculate the seismic source parameters if the seismic moment or the moment magnitude are available. The Global Centriod Moment Tensor (GCMT) earthquake catalog calculated the Mw of October 19, 2021 as 5.9. And defined the focal mechanism solution of its source as strike = 106°, dip= 76° and rake=-8° indicating a strike slip fault with normal component. Using the scaling relationship estimated by Kumar et al. (2017) to calculate the slip along the fault from the moment magnitude for strike-slip faulting earthquakes using Equation 3.

$$Log_{10} D = a+ b*Mw \quad (3)$$

Where, a= 0.558 (0.054), b=-4.032 (0.367) and Mw. Using the Mw and faulting mechanism defined by the GCMT the displacement along the fault is calculated as 0.18 meter. Wheras the average displacement from sentinel-1A of the study area is 0.14 meter, Also, the maximum average of vertical displacement is 0.26 m and the minimum average of vertical displacement is -0.12m.

5. Conclusions

This investigation seeks to calculate crustal displacement on the Western part of Nile Delta using SNAP processing derived from SAR images. The negative velocities are strongly localized across this region. The subsidence in cities near the Nile Delta can be attributed to the overload of urban structures, the collapse of loose soil, damaged buildings and roads, and ruptured pipes. In this section, the displacement range from −0.21 to +0.31 m/year. From two scenes (10 September -4 October 2021) the minimum value for the vertical deformation of two scenes is -0.14 m/year to the most considerable value for the movement of two scenes is 0.22 mm/year, was measured in the northern section. In two scenes (13-25 October 2021) the maximum displacement occurred in the southern sector, ranging from the smallest value for the movement of two scenes is -0.19 m/year, and the most significant value for the displacement of two scenes is 0.31 m/year. Also from two scenes (4-21 November 2021) the minimum value for the vertical deformation of two scenes is -0.21 m/year to the most considerable value for the movement of two scenes is 0.27 mm/year, was measured in the northern section. the displacement from seismicity data is calculated as 0.18 meter, Wheras the average displacement from sentinel-1A of the study area is 0.14 meter. Finally, authorities should adopt essential steps to regulate urban development in metropolitan areas and unsustainable water exploitation in the Westen Delta's desert margins to minimize the catastrophic effects of continuous land subsidence.

Acknowledgements

The authors are very grateful to the Reviewers, Editor in Chief Prof. Dr. Salih M. Awadh, the Secretary of Journal Mr. Sameer R. Ahmed, and the Technical Editors for their great efforts and valuable comments.

References

Aki, K., 1966. Generation and propagation of G waves from the Niigata earthquake of June 16, 1964. II. Estimation of earthquake movement, release energy, and stress-strain drop from G waves spectrum, Bulltein Earthquake Resources, 44, 23–88.

Ali, S.M. and Badreldin, H., 2019. Present-day stress field in Egypt based on a comprehensive and updated earthquake focal mechanisms catalog. Pure and Applied Geophysics, 176 (11), 4729-4760.

Badawy, A. 2005. Present-day seismicity, stress field and crustal deformation of Egyptian. Journal of Seismology, 9(3), 267-276.

Braun, A., & Veci, L. 2020. TOPS Interferometry Tutorial. Array Systems.

Bürgmann, R., Rosen, P. A., & Fielding, E. J. 2000. Synthetic aperture radar interferometry to measure Earth's surface topography and its deformation. Annual Review of Earth and Planetary Sciences, 28(1), 169-209.

Elsaka, B., Radwan, A. M., & Rashwan, M., 2020. Evaluation of Nile Delta-Mediterranean Sea conjunction using GPS, satellite-based gravity and altimetry datasets. Journal of Geoscience and Environment Protection, 8(02), 33.

Embabi, N. S., 2018. The Nile Delta, in landscapes and landforms of Egypt, 57-68.

Gebremichael, E., Sultan, M., Becker, R., El Bastawesy, M., Cherif, O., & Emil, M. 2018. Assessing land deformation and sea encroachment in the Nile Delta: a radar interferometric and inundation modeling approach. Journal of Geophysical Research: Solid Earth, 123(4), 3208-3224.

Goldstein, R. M., & Werner, C. L. 1998. Radar interferogram filtering for geophysical applications. Geophysical Research Letters, 25(21), 4035-4038.

Gupta, A., Ed.. 2008. Large Rivers: Geomorphology and Management. John Wiley & Sons.

Hooper, A., Segall, P., & Zebker, H. 2007. Persistent scatterer interferometric synthetic aperture radar for crustal deformation analysis, with application to Volcán Alcedo, Galápagos. Journal of Geophysical Research, 112(B7).

Kumar S., Thingbaijam, P., Martin, M., and Goda, K., 2017. New empirical earthquake source-scaling laws, BSSA, 107 (5), 2225–2246.

Loew, A., & Mauser, W. 2007. Generation of geometrically and radiometrically terrain corrected SAR image products. Remote Sensing of Environment, 106(3), 337-349.

Mahmoud, S. M. 2003. Seismicity and GPS-derived deformation in Egypt. Journal of Geodynamics, 35(3), 333-352.

Mohamed, A. S., Abubakr, M. M., Awad, M. H., Sakr, K. O., & Etman, M. S. 2021. Utilisation of GNSS and seismicity for monitoring crustal deformation of the northern part of the Nile Delta, Egypt. NRIAG Journal of Astronomy and Geophysics, 10(1), 1-9.

Nabawy, B., and Shehata, A., 2015. Integrated petrophysical and geological characterization for the Sidi Salem-Wakar sandstones, offshore Nile Delta, Egypt. Journal of African Earth Sciences, 110, 160-175.

Saleh, M., Sakr, K., Rashwan, M., El-Faragawy, K., & El-Dabaa, M. 2018. Crustal deformation of the southeastern corner of Egypt derived from geodetic data. NRIAG Journal of Astronomy and Geophysics, 7(2), 227-236.

Sarhan, M. & Hemdan, K. 1994. North Nile Delta structural setting and trapping mechanism. 12th Petroleum Conference of EGPC, 1, 18.

Sestini, G. 1989. Nile Delta: a review of depositional environments and geological history. Geological Society, London, Special Publications, 41(1), 99-127.

Skakun, S., Roger, J. C., Vermote, E. F., Masek, J. G., & Justice, C. O. 2017. Automatic sub-pixel co-registration of Landsat-8 operational land imager and Sentinel-2A multi-spectral instrument images using phase correlation and machine learning based mapping. International Journal of Digital Earth, 10(12), 1253-1269.

Stanley, D. J. & Warne, A. G. 1994. Worldwide initiation of Holocene marine deltas by deceleration of sea-level rise. Science, 265(5169), 228-231.

Ullo, S. L., Addabbo, P., Di Martire, D. D., Sica, S., Fiscante, N., Cicala, L., & Angelino, C. V. 2019. Application of DInSAR technique to high coherence Sentinel-1 images for dam monitoring and result validation through in situ measurements. IEEE Journal of Selected Topics in Applied Earth Observations and Remote Sensing, 12(3), 875-890.

Veci, L. 2015. TOPS Interferometry Tutorial Sentinel-1 Toolbox.

Zebker, H. A., Rosen, P. A., & Hensley, S. 1997. Atmospheric effects in interferometric synthetic aperture radar surface deformation and topographic maps. Journal of Geophysical Research, 102(B4), 7547-7563.

Zhang, Z., Wang, H., Xu, F., & Jin, Y. Q. 2017. Complex-valued convolutional neural network and its application in polarimetric SAR image classification. IEEE Transactions on Geoscience and Remote Sensing, 55(12), 7177-7188.